JOURNAL OF GEOPHYSICAL RESEARCH, VOL. 114, A07205, doi:10.1029/2008JA013949, 2009

DEMETER observations of transmitter-induced precipitation of inner radiation belt electrons

K. L. Graf,[1] U. S. Inan,[1] D. Piddyachiy,[1] P. Kulkarni,[1] M. Parrot,[2] and J. A. Sauvaud[3]

Received 25 November 2008; revised 18 March 2009; accepted 3 April 2009; published 3 July 2009.

[1] Near loss cone energetic electron flux increases induced by ground-based very low frequency (VLF) transmissions are observed directly via satellite-based detection. In 2 years of experiments ranging from 27 March 2006 through 2 April 2008 with the 21.4-kHz transmitter NPM in Lualualei, Hawaii, and the French satellite DEMETER (detection of electromagnetic emissions transmitted from earthquake regions), only a few cases of detection of individual pulses of transmitter-induced precipitation of inner radiation belt electrons have been realized. Analysis of the specific cases of detection allow comparison of precipitating flux with predictions based on ray-tracing analyses of wave propagation and test particle modeling of the wave-particle interaction. Results indicate that the precipitated flux of >100 keV electrons induced by the NPM transmitter peaks at $L \simeq 1.9$ and, in the rare cases of detection, may be at higher energies than the ~100 keV peak predicted by the model. The low detection rate is attributed to the orientation of the DEMETER particle detector, which is mostly overwhelmed by the trapped population at the location of detection.

Citation: Graf, K. L., U. S. Inan, D. Piddyachiy, P. Kulkarni, M. Parrot, and J. A. Sauvaud (2009), DEMETER observations of transmitter-induced precipitation of inner radiation belt electrons, *J. Geophys. Res.*, *114*, A07205, doi:10.1029/2008JA013949.

1. Introduction

[2] Energetic electrons trapped by the Earth's magnetic field make up the radiation belts. The sources, losses and dynamics of energetic electrons in these radiation belts is a topic which has received considerable attention [*Friedel et al.*, 2002; *Shprits et al.*, 2008a, 2008b]. Pitch angle scattering in wave-particle interactions involving whistler mode waves is one of the dominant loss mechanisms. Past work has demonstrated the capability of ground-based VLF transmitters to precipitate energetic electrons [*Vampola*, 1977; *Imhof et al.*, 1981; *Koons et al.*, 1981] and global diffusion studies have indicated the importance of ground-based VLF transmitters in determining long-term energetic electron lifetimes in the inner radiation belt [*Abel and Thorne*, 1998]. We present herein the initial results of an experiment aimed at direct measurement of transient bursts of energetic electrons scattered into the bounce loss cone by nonducted VLF waves from the NPM transmitter in Lualualei, HI. "NPM" is the three-letter call sign of this Naval VLF transmitter. For convenience, Naval VLF transmitters will be referred to by their call signs throughout this paper. Preliminary results involving indirect detection via subionospheric VLF observation techniques of the ionospheric effects of energetic electron precipitation were presented by *Inan et al.* [2007b].

[3] The Stimulated Emission of Energetic Particles (SEEP) experiment conducted by Lockheed Palo Alto Research Laboratories and Stanford University provided direct observation of bursts of transmitter-induced precipitation [*Imhof et al.*, 1983; *Inan et al.*, 1985] induced by the NAA transmitter (44.7°N, 67.3°E, $L = 2.85$) in Cutler, ME, but a body of long-term results to quantify the full global extent of the phenomena has yet to be compiled. Additionally, such past work focused on higher-latitude transmitters where the corresponding resonant electron energies are in the range of tens of keV, and NAA, the primary transmitter, is located at a longitude near the South Atlantic Anomaly (SAA) where the mirror point conjugate to the location of satellite-based detection is below sea level [*Imhof et al.*, 1983]. The NPM transmitter utilized for the current study is at a much lower latitude, with corresponding resonant electron energies being >100 keV, and is located in the Pacific sector significantly east of the SAA such that there is a considerable difference between the drift and bounce loss cones at its geomagnetic longitude.

[4] Experiments were conducted with coordinated DEMETER passes between 27 March 2006 and 2 April 2008. Measurements are recorded onboard the DEMETER satellite, on which both lightning-induced electron precipitation [*Inan et al.*, 2007a] and transmitter-induced electron precipitation events have previously been observed [*Sauvaud et al.*, 2008]. Examples of coordinated transmitter-induced precipitation events detected onboard DEMETER are presented along with a description of the observation statistics

[1] Space, Telecommunications and Radioscience Laboratory, Stanford University, Stanford, California, USA.
[2] Laboratoire de Physique et Chimie de l'Environnement, Centre National de la Recherche Scientifique, Orléans, France.
[3] Centre d'Etude Spatiale des Rayonnements, Centre National de la Recherche Scientifique, Toulouse, France.

0148-0227/09/2008JA013949$09.00

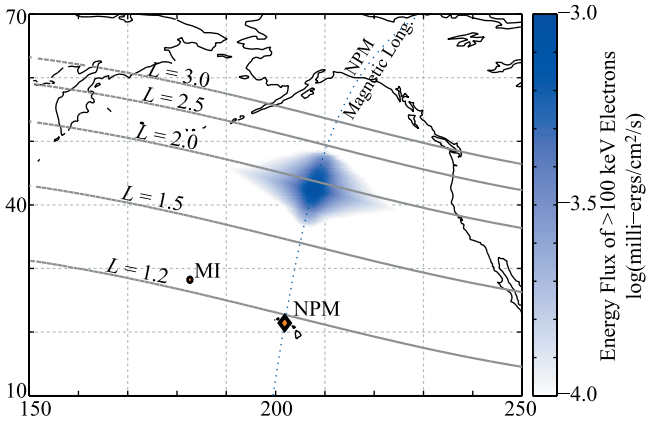

Figure 1. Location and magnitude of predicted NPM-induced precipitation region with the locations of the NPM transmitter and Midway Island (MI) receiver marked.

from the 2-year study and a comparative theoretical analysis of the results.

2. Experimental Procedure

[5] During the course of this experiment, the U.S. Navy 424 kW, 21.4 kHz VLF transmitter NPM located at Lualualei, HI (21.4°N, 158.2°W; L = 1.17) was keyed ON/OFF in periodic formats for two 30-min periods each day. These transmission periods were selected to correspond to the traverses of the DEMETER satellite through the regions of expected precipitation or its corresponding conjugate, during which measurements of both electromagnetic field and energetic particle fluxes were recorded on DEMETER. The data are analyzed for correlations between NPM transmission bursts and particle flux bursts to identify cases of NPM-induced precipitation.

[6] The majority of the transmissions were keyed in a 5-sec ON/5-sec OFF format. This means NPM transmitted its 21.4 kHz signal at nearly full power for 5 sec, then turned off for 5 sec, and repeated this cycle for the duration of the 30-min keying period. A VLF receiver stationed at 28.21°N, 177.38°W on Midway Island (MI) provided confirmation of NPM transmissions as well as observations of the ionospheric effects of NPM-induced precipitation with the subionospheric VLF method [*Inan et al.*, 2007b]. Experiments were conducted nightly from 27 March 2006 through 2 April 2008, with measurements taking place on roughly one third of the days in coordination with passes of the satellite DEMETER. There were occasional breaks in experimentation due to high onboard memory usage in burst mode and the need to shift emphasis to other experiments conducted with DEMETER. The largest break occurred from 26 October 2006 through 10 April 2007, with no DEMETER recordings in burst mode being available.

[7] The predicted energetic electron precipitation region induced by NPM is shown in Figure 1, as determined using a VLF ray tracing code and a test particle model of the wave particle interaction which is further discussed in section 5. According to the model, peak precipitation of >100 keV electrons is expected to occur at L = 1.9 with a full-width half-maximum (FWHM) of approximately 0.3 L spanning the range L = 1.7–2.0. DEMETER passes through this precipitation region and its conjugate roughly once per day, south to north, traversing the FWHM of the precipitation region in approximately 2 min.

[8] DEMETER is a microsatellite developed by the French National Center for Space Studies (CNES) with a ~700 km altitude, 98.3° inclination orbit [*Parrot*, 2006]. An onboard electric field instrument (ICE) measures electric field fluctuations of up to 20 kHz in burst mode, and an instrument for particle detection (IDP [*Sauvaud et al.*, 2006]) measures 72.9 keV–2.35 MeV electrons with 8.9 keV resolution in burst mode at one sample per second. The 21.4 kHz transmission frequency of NPM places it above the cutoff of the ICE, but a powerful aliased signal is still received at 18.6 kHz. A correction factor of 2.7, which was determined from the filter characteristic of the ICE, is applied to the aliased signal to calculate the electric field strength of the NPM transmission at the location of DEMETER. The IDP collimator views ~30° FWHM perpendicular to the orbital plane with a geometric factor of 1 cm^{2}str. During its passes through the NPM precipitation region, the IDP consistently points ~77.0° east of north. The Earth's local magnetic field, according to IGRF/DGRF model data, is approximately H = 17.1 μT, Z = 29.3 μT, D = 13.6°, where H is the horizontal component of the field, Z is the vertical component (positive downward), and D is the declination of the field (positive eastward). Given these parameters and their variations, the angle θ_N between the IDP and the Earth's magnetic field at this location is typically within 0.1° of 77.9°, so the IDP views the local pitch angle range of ~62.9°–92.9°. In the conjugate region, the IDP points ~76.8° east of north and the local magnetic field is approximately H = 17.9 μT, Z = −32.8 μT, D = 20.6°. The angle θ_S between the IDP and the local magnetic field in the conjugate region is ~75.8°, so the IDP views the local pitch angle range of ~60.8°–90.8°. As such, the DEMETER IDP views primarily the locally trapped particles, and does not provide a direct measurement of precipitating energetic particle flux. Nevertheless, perturbations in its measurements still serve as an indication of scattering events and can provide an estimate of precipitation flux upon additional calculations. Together, the ICE and the IDP of DEMETER provide in situ measurements of both the NPM transmissions and the energetic particle flux. We will use these measurements to study NPM-induced precipitation.

3. Observations

3.1. Standard Formats

[9] During selected few DEMETER passes through the NPM precipitation region and its conjugate with NPM transmitting in a periodic ON-OFF format, significant bursts of energetic particle flux were detected by DEMETER in correlation with NPM ON transmissions. Sample cases of detection are presented with their key features described. Analysis and Discussion of the results is reserved for sections 4–6.

[10] The first case of detection occurred on 29 December 2005 and is presented in Figure 2. On 29 December 2005 between 07:20:05 and 07:20:30 UT, DEMETER passed through the NPM precipitation region approximately 730 km east of its predicted center 10 min after the

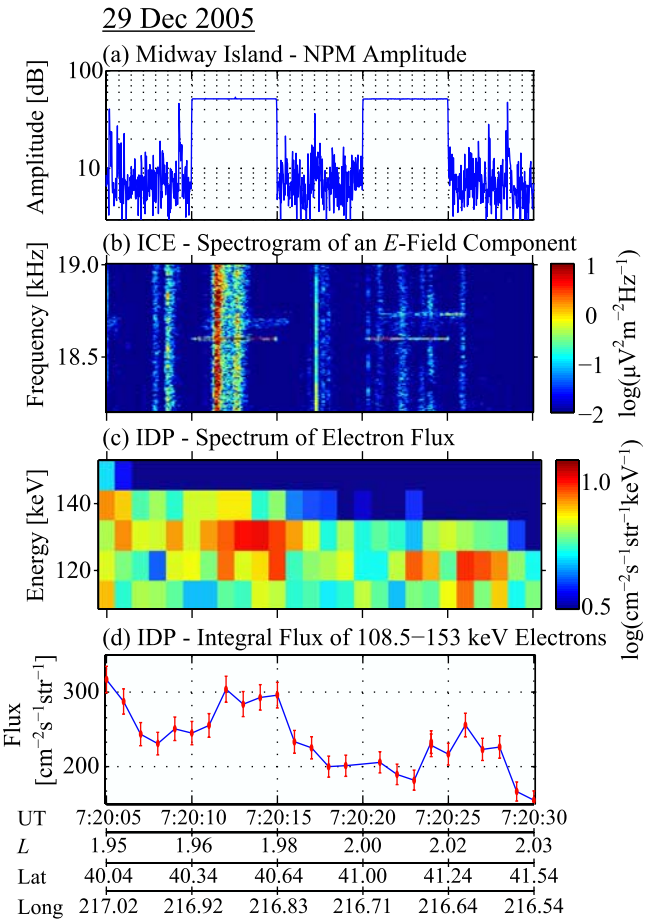

Figure 2. Results summary for 29 December 2005. (a) Magnetic field amplitude detected in the NPM frequency channel by the MI receiver showing the 5-sec ON/5-sec OFF transmission format. (b) Spectrogram of electric field measured by DEMETER showing an aliased image of the NPM signal. (c) Spectrum of near loss cone energetic electron flux as detected onboard DEMETER showing two bursts of particle flux closely following NPM ON transmissions. (d) Integral flux of the energetic electron flux plotted in Figure 2c. The bursts in near loss cone energetic electron flux correlated with NPM ON transmissions suggest the detection of NPM-induced precipitation.

commencement of NPM keying. NPM transmitted in a 5-sec ON/5-sec OFF format as confirmed by VLF data from MI. DEMETER ICE data exhibited the same NPM transmission format at its 700 km orbit and the IDP recorded two bursts of energetic particle flux near L = 2.0 in the 108.5–144.1 keV energy range. The first burst was centered at ~130 keV while the second, recorded at a higher L shell, occurred at ~120 keV. The bursts were each of 5 to 6 sec in duration and each followed within 3 ± 1 sec of the start of an NPM ON transmission. The 1-sec time resolution of the IDP instrument did not allow for more accurate determination of delay times. DEMETER started recording burst mode data for this pass at 07:20:05 UT, which is the start time for the plots of Figure 2. The significant energetic particle flux which was measured in the opening seconds of this record period may have been due to the NPM ON transmission which ended at 07:20:05 UT, but this cannot be stated definitively since data for that preceding transmission period were not captured by our data set. After the 25-sec window shown here, no other such bursts of energetic particle flux were detected during this pass.

[11] A similar case occurred on 3 September 2007 between 10:05:45 and 10:06:10 UT; this time in the conjugate precipitation region with DEMETER passing within 50 km of the center of the predicted region 21 min into the 30 min NPM keying session. This case is presented in Figure 3. NPM once again transmitted a 5-sec ON/5-sec OFF format. This NPM transmission was detected in DEMETER ICE data in the form of two pulses at two distinct frequencies for each 5-sec pulse, and the transmission was confirmed in the VLF data from MI. The persistent noise received at 18.6 kHz by the ICE in the southern hemisphere on this day was likely due in part to the 18.6 kHz transmitter NST located in

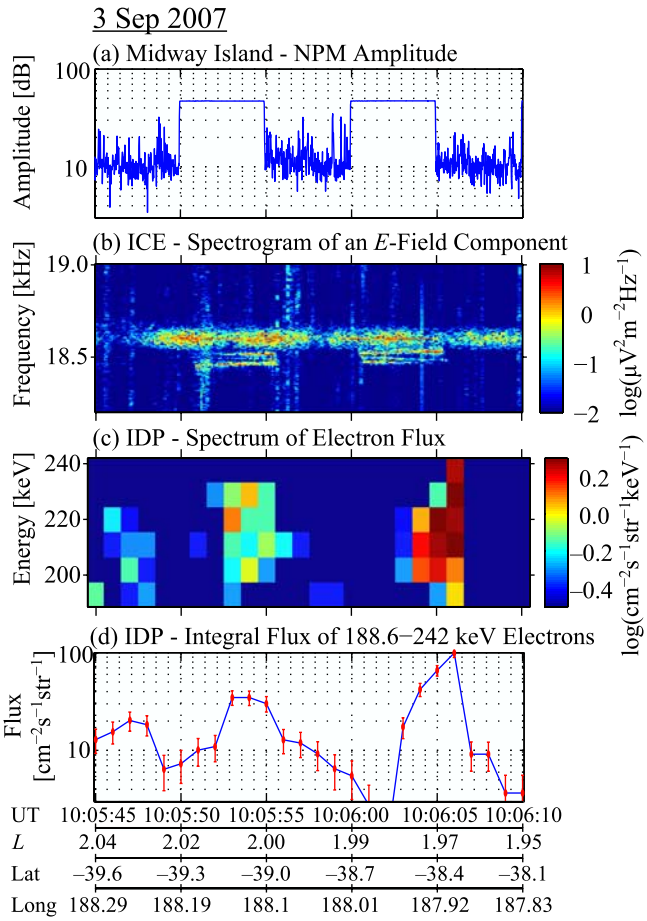

Figure 3. Results summary for 3 September 2007. (a) Magnetic field amplitude detected in the NPM frequency channel by the MI receiver showing the 5-sec ON/5-sec OFF transmission format. (b) Spectrogram of electric field measured by DEMETER in the conjugate region showing a Doppler shifted aliased image of the NPM signal. (c) Spectrum of near loss cone energetic electron flux as detected onboard DEMETER showing two bursts of particle flux closely following NPM ON transmissions. (d) Integral flux of the energetic electron flux plotted in Figure 3c. The bursts in near loss cone energetic electron flux correlated with NPM ON transmissions suggest the detection of NPM-induced precipitation.

Table 1. Results of Analyzing the 194 DEMETER Passes When NPM was Transmitting in a 5-sec ON/5-sec OFF Format for NPM-Correlated Bursts of Energetic Particle Flux

	Number of Occurrences in Precipitation Region	Number of Occurrences in Conjugate Region
2 Correlated bursts	3	2
1 Correlated burst	9	13
No bursts detected	73	82
1 Uncorrelated burst	5	6
2 Uncorrelated bursts	1	0
Total number of passes	91	103

Woodside, Australia (38.5°S, 146.9°E; L = 2.34). The multipulse configuration of the received NPM signal was a manifestation of Doppler shift resulting from the satellite motion [*Starks et al.*, 2009]. One of the pulses was the signal which first propagated in the Earth ionosphere waveguide to the southern hemisphere and leaked upward to the satellite altitude therein. The other pulse was the signal which entered the magnetosphere in the North, and then propagated to the southern hemisphere in a non-ducted, nearly field-aligned path. This second pulse would arrive in the conjugate region with a relatively high wave normal angle (and thus a high refractive index), oriented nearly horizontal along the satellite trajectory, thus leading to a large Doppler shift. Doppler shifted pulses were also visible in Figure 2, but the Doppler shifted pulse was much weaker in that case because detection was taking place in the northern hemisphere. Near L = 2.0, two bursts of energetic particle flux were detected in the 188.6–242 keV energy range, with no noticeable change in energy spectrum occurring between the two bursts. The bursts were each of 3 to 5 sec in duration and each followed within 3 ± 1 sec of the start of an NPM ON transmission. Outside of the 25 sec window discussed here, no other such bursts of energetic particle flux were detected during this pass.

[12] This type of transmission format and associated detection technique comprised the majority of the NPM keying experiments during DEMETER passes. DEMETER traversed the precipitation region too rapidly with the background energetic particle flux varying too significantly for superposed epoch or Fourier analysis of the IDP data to be effective. The 1-sec time resolution of the IDP made detection more difficult with faster transmission formats like 1-sec ON/1-sec OFF, and the quick pass through the precipitation region made the slower transmission formats such as 10-sec ON/10-sec OFF less effective. As a result, 194 of the 211 passes utilized the 5-sec ON/5-sec OFF format. Of these 194 passes, 91 were through the precipitation region and 103 were through its conjugate in the southern hemisphere.

[13] All passes were analyzed for potential signatures of NPM-induced precipitation using the detection technique detailed for the two cases above. If a significant burst in energetic particle flux lasted for 3 to 6 sec and started within 3 sec of the start of an NPM ON transmission, it was counted as correlated with NPM transmission and qualified as potentially NPM-induced precipitation. If such a burst in energetic particle flux started 4 to 9 sec after the start of an NPM ON transmission, it was counted as uncorrelated with NPM transmissions and was not considered to have been potentially caused by NPM. The results of this analysis are presented in Table 1. The majority of the cases of detection occurred for energetic electrons in the 100–200 keV range, with detection occasionally occurring in the 200–250 keV range. For the sake of completeness, the data were also analyzed for the correlation of flux decreases with NPM transmissions, but no instances of such correlation were found.

3.2. Special Formats

[14] There were a number of other transmission formats attempted over the course of the experiments that were not included in the overall results discussed above. One of these was a 5-min ON/1-min OFF format designed to allow the drift loss cone to empty and subsequently turn NPM ON just as DEMETER passed through the precipitation region. This type of transmission format was used during six DEMETER passes, and data from two of the six exhibited correlation of an increase in energetic particle flux with NPM ON transmission. One of these occurred on 20 February 2008 and is presented in Figure 4.

[15] On 20 February 2008 between 07:19:30 and 07:22:30 UT, DEMETER passed through the NPM precipitation region approximately 450 km east of its predicted center. NPM transmitted a 5-min ON/1-min OFF format as detected both with the VLF receiver at MI and onboard DEMETER with the ICE. NPM turned from ON to OFF when DEMETER was near L = 1.65 and a slight, but not statistically significant, decrease in energetic particle flux in the 99.6–144.1 keV energy range followed within 30 sec. NPM turned back ON when DEMETER was near L = 1.8 and a significant increase in energetic particle flux immediately followed. The energy of this flux enhancement proceeded to decrease with increasing L.

4. Analysis

[16] An analysis of the IDP viewing window in relation to the trapped and precipitating radiation belt particles is critical for proper interpretation of the experimental results. The IDP possesses a FWHM of ~30°, and the angle between the IDP and the local magnetic field of the Earth is θ_N = 77.9° in the northern hemisphere NPM precipitation region and θ_S = 75.8° in the conjugate region. These two configurations are close enough that an in-depth analysis of just the northern precipitation region is sufficient for an understanding of both. Comparisons are drawn between this analysis and the clearest case of DEMETER measurements of 29 December 2005. For these purposes, it is shown in Figure 5 that the differential flux in the 130.75 keV energy bin increases from an average of 6.6 cm^{-2} s^{-1} str^{-1} keV^{-1} for NPM OFF to 10.2 cm^{-2} s^{-1} str^{-1} keV^{-1} for NPM ON. These correspond to IDP counting rates of 59.0 s^{-1} and 90.5 s^{-1}, respectively.

[17] In the precipitation region, the IDP detects particles of local pitch angles ~62.9°–92.9°. By combining the expression for a dipole magnetic field with the first adiabatic invariant, these local pitch angles are related to equatorial pitch angles through:

$$\alpha_{eq} = \sin^{-1}\sqrt{\sin^2\alpha\,\frac{\cos^6\lambda}{\sqrt{1+3\sin^2\lambda}}} \qquad (1)$$

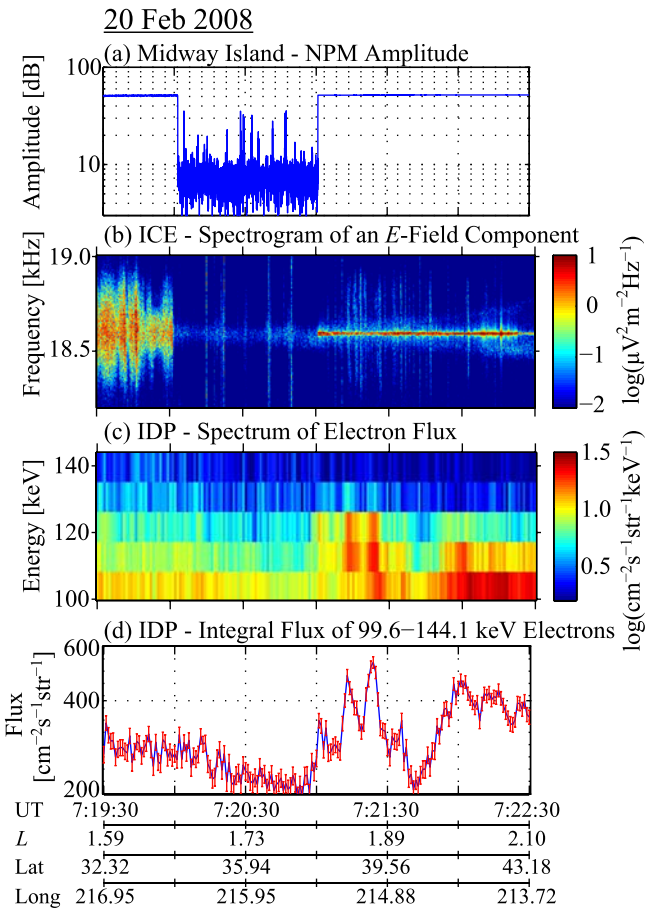

Figure 4. Results summary for 20 February 2008. (a) Magnetic field amplitude detected in the NPM frequency channel by the MI receiver showing the 1-min OFF/5-min ON transmission format. (b) Spectrogram of electric field measured by DEMETER showing an aliased image of the NPM signal. (c) Spectrum of near loss cone energetic electron flux as detected onboard DEMETER showing an increase correlated with NPM turning ON at 07:21:00 UT. (d) Integral flux of the energetic electron flux plotted in Figure 4c. The increase in near loss cone energetic electron flux correlated with NPM turning ON suggests the detection of NPM-induced precipitation.

where λ is the local geomagnetic latitude, α is the local pitch angle, and α_{eq} is the equatorial pitch angle. The corrected geomagnetic latitude at the location of DEMETER is 41.49° for $L = 2.0$, and it is determined that the IDP thus views equatorial pitch angles ~17.7°–19.9°. Given that the bounce loss cone and drift loss cone angles at the geomagnetic longitude of NPM are ~16.86° and ~23.5° respectively, it is clear that DEMETER in fact measures particles that are still trapped, but which are destined to precipitate at the South Atlantic Anomaly. In other words, particles detected by DEMETER at 700 km altitude possess pitch angles such that they mirror prior to interacting with the denser regions of the ionosphere. While this presents a background flux which can hinder the detection of precipitation events, the detection of bursts of energetic particle flux on DEMETER is still an indicator of pitch angle scattering and eventual precipitation, as is shown with our modeling below.

[18] The illustrative model presented here consists of three main steps: (1) The evaluation of the counting rate (CR) integral for the IDP for the case of a typical equatorial differential directional flux $j(\alpha_{eq}, E)$. (2) The simulation of scattering by perturbing $j(\alpha_{eq}, E)$. (3) The recalculation of the CR integral and the determination of the precipitated flux for the scattered $j(\alpha_{eq}, E)$. Additional steps appear in the conversions between local and equatorial pitch angles and in scaling to match experiment and established models. In order to simplify the procedure, $j(\alpha_{eq}, E)$ is approximated as a scalable pitch angle distribution $j(\alpha_{eq})$. This approximation is valid for comparisons to our experimental results because the flux measurements appear in discrete energy bins of 8.9 keV resolution, so we can interpret j as $j(\alpha_{eq}, E_{min} < E < E_{max}) = j(\alpha_{eq})$ by assuming the distribution to be uniform over our chosen energy bin.

[19] Four equatorial pitch angle distributions (PADs) are presented: square, sine, anisotropic, and shifted. Respectively, these are defined as

$$j_1(\alpha_{eq}) = a_0\rho_1\, u\left(\alpha_{eq} - \alpha_{eq}^{lc}\right) \tag{2}$$

$$j_2(\alpha_{eq}) = a_0\rho_2 u\left(\alpha_{eq} - \alpha_{eq}^{lc}\right)\, \sin(\gamma_1) \tag{3}$$

$$j_3(\alpha_{eq}) = a_0\rho_3 u\left(\alpha_{eq} - \alpha_{eq}^{lc}\right)\left[0.2\sin^{0.4}(\gamma_1) + 0.8\sin^{10}(\gamma_1)\right] \tag{4}$$

$$j_4(\alpha_{eq}) = a_0\rho_4\left\{10^{-4} u\left(\alpha_{eq} - \alpha_{eq}^{lc}\right)\sin^{0.2}(\gamma_1) + u\left(\alpha_{eq} - \alpha_{eq}^{c}\right)\left[0.46\sin^{0.57}(\gamma_2) + 0.14\sin^{12}(\gamma_2)\right]\right\} \tag{5}$$

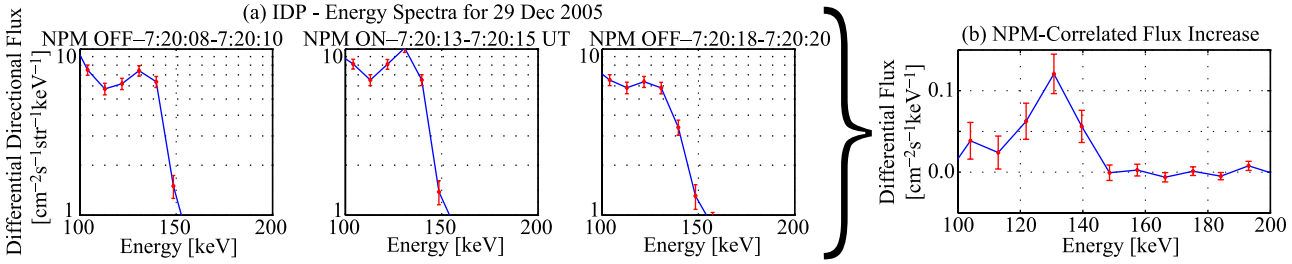

Figure 5. (a) Energy spectra of near loss cone energetic electron flux as detected onboard DEMETER on 29 December 2005. (b) An estimate of the NPM-correlated flux increase computed by subtracting the average of the adjacent OFF windows of Figure 5a from the ON window and converting to $cm^{-2}\,s^{-1}\,keV^{-1}$.

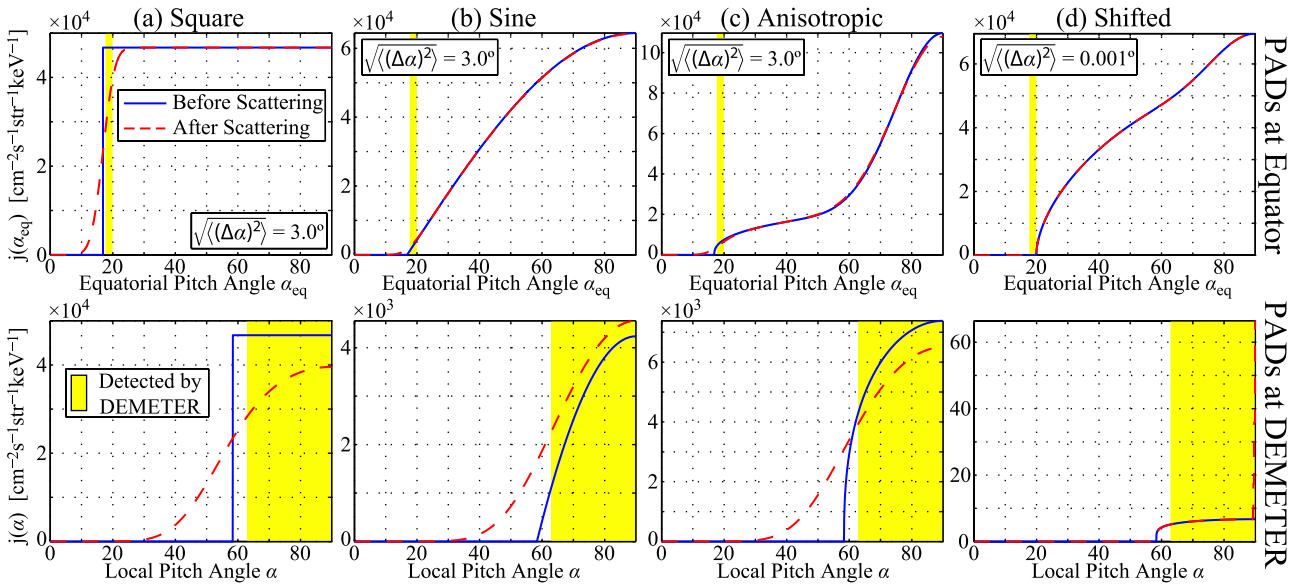

Figure 6. Four modeled pitch angle distributions (PADs; square, sine, anisotropic, and shifted) with pitch angles detected by DEMETER highlighted, plotted both at the equator and at the $L = 2.0$, $\lambda = 41.49°$ location of DEMETER in the precipitation region. Scattering is simulated by convolving the equatorial PAD with a Gaussian distribution whose width is defined by the RMS pitch angle scatter.

$$\gamma_1 = \left(\alpha_{eq} - \alpha_{eq}^{lc}\right)\left(\frac{\pi/2}{\pi/2 - \alpha_{eq}^{lc}}\right)$$

$$\gamma_2 = \left(\alpha_{eq} - \alpha_{eq}^{c}\right)\left(\frac{\pi/2}{\pi/2 - \alpha_{eq}^{c}}\right)$$

where $\alpha_{eq}^{lc} = 16.86°$ is the bounce loss cone angle, u(·) is the unit step function, a_0 is a scalable constant determined by the differential flux, and each ρ is a constant chosen such that $\int_0^{\pi}(j(\alpha_{eq})/a_0)\sin(\alpha_{eq})d\alpha_{eq} = 1$. Therefore $\rho_1 \simeq 0.52$, $\rho_2 \simeq 0.72$, $\rho_3 \simeq 1.23$, and $\rho_4 \simeq 1.30$. In equation (5), $\alpha_{eq}^{c} \simeq 19.92°$ provides a shifted cutoff just outside the IDP viewing window. These equatorial PADs are shown in the first row of Figure 6. The first three are representative PADs, close variants of which commonly appear in radiation belt analysis [e.g., *Anderson*, 1976; *Inan*, 1977; *Inan et al.*, 1978]. Most quiet time PADs tend to fall somewhere between the sine and the anisotropic distributions [*Lyons and Williams*, 1975]. The structure of the shifted PAD is designed to fall in between those of the sine and the anisotropic distributions, but its key feature is that its primary cutoff is shifted from α_{eq}^{lc} to just beyond the IDP viewing window with only a very small tail extending to α_{eq}^{lc}. This shifted PAD is designed to match the experimental results discussed here and is representative of a PAD whose drift loss cone is relatively empty. All distributions are assumed to be azimuthally invariant.

[20] For comparison to the experimental results of 29 December 2005, the case of 130 keV particles at $L = 2.0$ is considered. According to the AE8 radiation belt model, the equatorial, omnidirectional differential flux for these parameters is 5.62×10^5 cm^{-2}s^{-1}keV^{-1} at solar minimum. Since this value must match $\int_0^{2\pi}\int_0^{\pi} j(\alpha_{eq})\sin(\alpha_{eq})\, d\alpha\, d\phi$, it is determined that $a_0 \simeq 89.4 \times 10^3$ cm^{-2}s^{-1} str^{-1} keV^{-1}.

[21] With the PADs defined and the $\alpha \leftrightarrow \alpha_{eq}$ relation of equation (1), the CR of the IDP located at $L = 2.0$, $\lambda = 41.49°$ with orientation $\theta_N = 77.9°$ is calculated following the formulation of *Walt* [1994]:

$$CR = E_{bin}\int_0^{2\pi}\int_0^{\beta} j(\alpha)A\cos(\eta)\sin(\eta)d\eta\, d\psi \qquad (6)$$

where, $A = 4.67$ cm^2 is the IDP area, $E_{bin} = 8.9$ keV is the energy resolution, $\beta = 15°$ is the IDP half-width half-maximum, and the coordinate system has been transformed from that which is oriented along the magnetic field vector to that which is orientated along the direction of the IDP through use of the cosine law for spherical triangles. In this new coordinate system, η is the polar angle measured from the IDP vector and ψ is the azimuthal angle.

[22] Next, the resultant pitch angle scattering is approximately estimated by convolving the equatorial PAD with a normalized Gaussian distribution. The standard deviation of the Gaussian effectively represents the root mean square (RMS) pitch angle change $\sqrt{\langle(\Delta\alpha)^2\rangle}$. By estimating the wave parameters of the NPM signal in the magnetosphere as calculated in the model of section 5 and following the formulations of *Inan* [1987] for scattering by coherent waves, the RMS pitch angle change is found to be $\sim$0.001°.

[23] Once a scattered equatorial PAD $j_{scat}(\alpha_{eq})$ is calculated, it is transformed to the detector location using equation (1) and the CR integral is recalculated using equation (6). The precipitation flux can be calculated by transforming $j_{scat}(\alpha_{eq})$ to the height of the upper ionosphere and calculating the downward-propagating flux at that location. Alternatively, the precipitation flux can be calculated directly from the equatorial distribution by following the formulations of *Ristić-Djurović et al.* [1998] and *Lauben*

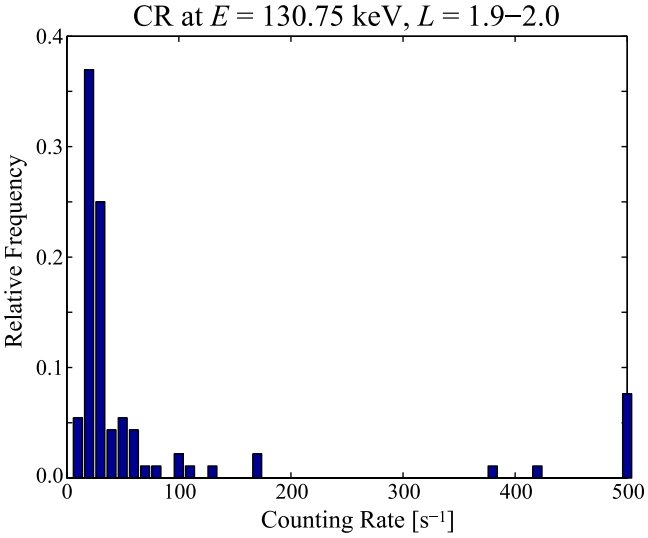

Figure 7. Distribution of average counting rates measured by DEMETER while traversing L = 1.9–2.0 of the NPM precipitation region. All outliers beyond the maximum value of the plot are grouped in the final bin.

et al. [2001] which adjust for solid angle and flux tube compression:

$$N = 2\pi \sin^{-2}\left(\alpha_{eq}^{lc}\right)\int_0^{\alpha_{eq}^{lc}} j_{scat}(\alpha_{eq})\cos(\alpha_{eq})\sin(\alpha_{eq})d\alpha_{eq} \quad (7)$$

[24] The basic functionality of this illustrative model has been validated in two ways: (1) Precipitation flux is calculated using both methods discussed above in order to verify agreement and confirm that the coordinate transformations and numerical integrations required for the counting rate integrals were implemented properly. (2) For the case of a sine PAD with NPM transmitting, inducing an estimated 0.001° RMS pitch angle change, the results are directly compared to the results of the precipitation model of *Kulkarni et al.* [2008] which is discussed in section 5. At the L = 2.0, E = 130 keV for which the scaling factors of this section have been calibrated, both models predict the precipitation flux to be $\sim 10^{-4}$ cm^{-2} s^{-1} keV^{-1}.

[25] Figure 6 shows the four PADs before and after scattering, plotted both at the equator and at the location of DEMETER. For illustrative purposes in the plots, the standard deviation used to define the Gaussian for scattering the square, sine, and anisotropic PADs is 3.0°. The more realistic value of 0.001° is used for scattering the shifted distribution. The square and sine PADs illustrate the effects which pitch angle scattering can have on the IDP measurements. The square PAD clearly leads to the highest precipitation flux, producing ~18 times the precipitation of the sine PAD for $\sqrt{\langle(\Delta\alpha)^2\rangle} \simeq 3.0°$, but it actually leads to a decrease in the Counting Rate Integral. Recall that the IDP views local pitch angles ~62.9°–92.9°, corresponding to equatorial pitch angles ~17.7°–19.9°, and particles are scattered away from these angles for a square PAD leading to a decrease in CR by 21%. For a sine PAD, the particles scattered into the near loss cone region increase the CR by 15%. As was pointed out by *Inan et al.* [1978], the anisotropic PAD behaves approximately like a scaled square PAD near the loss cone, and its CR decreases by 13%. Note that these CR changes are for $\sqrt{\langle(\Delta\alpha)^2\rangle} \simeq 3.0°$; if this value is instead set to 0.001°, all of these CR changes fall to significantly less than 1%. These small percentage changes in CR would not be detectable over normal fluctuations without substantial averaging. The histogram of Figure 7 shows that the CR for about half of the IDP measurements is less than 36 s^{-1}. Even a 15% change in this CR would be less than the standard deviation of the measurement. Considering that the actual change is likely to be much less than 1%, only the most extreme of the observed cases would produce a positive detection for either of these PADs.

[26] The fact that not one of PADs equations (2)–(4) with their edges at the bounce loss cone can produce a positive detection on DEMETER is in agreement with the low rate of detection seen in the experimental results. However, these distributions are flawed in that they produce significantly higher CR levels than are measured by DEMETER. For example, the sine PAD, scaled to match the AE8 model for 130 keV electrons as described above, produces a CR of 29×10^3 s^{-1}. The square PAD, 408×10^3 s^{-1}. These values are roughly 10^3 and 10^4 times greater than a typical CR. The shifted PAD corrects this issue by having a nearly square tail scaled by 10^{-4} extend to the bounce loss cone while the bulk of the distribution is shifted to just beyond the viewing window of the IDP facilitating a significant CR increase following scattering. For the shifted PAD in Figure 6d, the CR changes from 55.9 s^{-1} before scattering to 85.5 s^{-1} after scattering. These CR values are generated using the realistic $\sqrt{\langle(\Delta\alpha)^2\rangle} \simeq 0.001°$ and they closely mirror the measured CR values for 29 December 2005, which were 59.0 s^{-1} for NPM OFF and 90.5 s^{-1} for NPM ON.

[27] It is clear from this analysis that the detection of NPM-induced pitch angle scattering onboard DEMETER is possible, but requires a very specific PAD. The detection of pitch angle scattering at the angles viewed by DEMETER would suggest comparable pitch angle scattering of near loss cone particles, meaning that some particles would precipitate if near loss cone particles are present in the PAD. Such detection of pitch angle scattering also requires favorable wave propagation considering that the wave magnetic field strength used in the RMS pitch angle change calculation is a relatively high estimate, according to recent modeling by *Lehtinen and Inan* [2008]. To summarize, typical scattering events in the presence of most PADs would produce precipitation without causing a noticeable change in the flux measurements of the DEMETER IDP for the precipitation regions considered here. Therefore the rarity of the observations on DEMETER is largely attributed to the orientation of the IDP, which primarily views the trapped particle population and is thus only capable of detecting a scattering event in the presence of particular PADs.

5. Comparison to Model

[28] While the experimental results were compared to an illustrative model in the previous section in order to gain insight into DEMETER IDP measurements, in this section we compare the results to a much more detailed model. As is mentioned by *Inan et al.* [2007b], and is discussed in

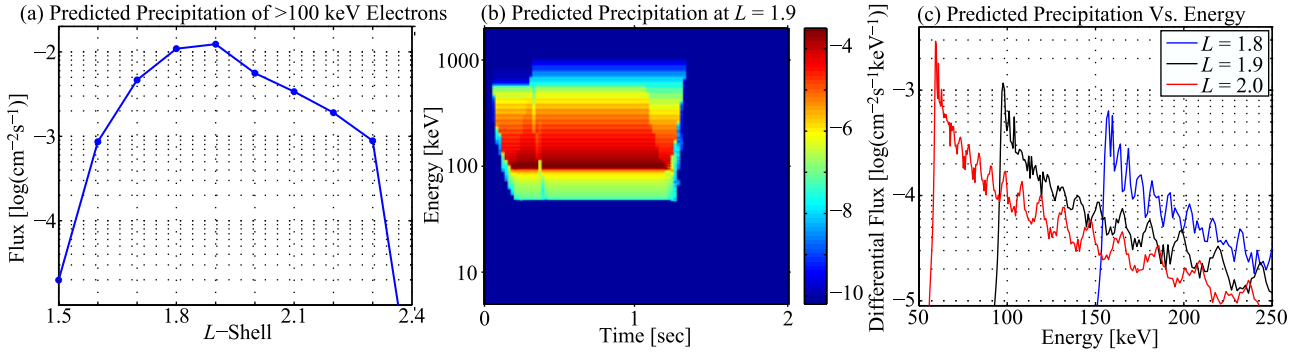

Figure 8. Simulation results. (a) Predicted distribution of NPM-induced precipitation of >100 keV electrons L. (b) Predicted precipitation at $L = 1.9$ as a function of energy and time for a 1-sec burst of transmission by the NPM transmitter starting at time $t = 0$. (c) Predicted precipitation versus energy plotted for $L = 1.8$, 1.9, and 2.0 showing peak energies and flux levels.

more detail by *Kulkarni et al.* [2008], a model of wave-induced electron precipitation is used to model the precipitation induced by the NPM transmitter. In this model, whistler wave propagation in the magnetosphere is simulated using the Stanford ray tracing code [*Inan and Bell*, 1977], including Landau damping effects in accordance with the theoretical formulation of *Brinca* [1972]. The plasmaspheric cold plasma density is based on the work of *Carpenter and Anderson* [1992], while the energetic particle populations (with a sine pitch angle distribution) are based on the (solar minimum) AE8 fluxes. Pitch angle scattering of energetic particles into the loss cone by the whistler wave is calculated according to the work of *Bortnik et al.* [2006], and yields precipitated flux as a function of energy, L shell, longitude, and time. Parameters of the NPM transmitter as discussed in section 2 serve as inputs to the model, and the bandwidth of the signal is estimated to be ~3 Hz based on DEMETER measurements. The results of the model are summarized in Figure 8 and are briefly presented here. A more thorough discussion of the model and its results are available in the work of *Kulkarni et al.* [2008] and references therein.

[29] According to the model, peak precipitation of >100 keV electrons occurs at $L = 1.9$ with an FWHM of approximately 0.3 L spanning $L = 1.7–2.0$. The precipitation peaks near a resonant energy which decreases with increasing L shell, occurring near 157 keV at $L = 1.8$, 98 keV at $L = 1.9$, and 59 keV at $L = 2.0$. At $L = 1.9$, the peak precipitation flux is 1.17×10^{-3} cm^{-2}s^{-1}keV^{-1}. While these results are for a sine PAD with AE8 scaling, results from this same model were presented by *Inan et al.* [2007b] for a square PAD and for energetic particle populations based on observations from the POLAR spacecraft [*Bell et al.*, 2002]. The use of a square PAD leads to higher values of precipitation flux, but the distribution of that flux in energy, L shell, longitude, and time remains largely unchanged.

[30] As discussed in section 4, the results of this model cannot be directly compared to experiment because DEMETER does not directly measure the flux of precipitating particles. In order to attempt an indirect comparison, the shifted PAD of Figure 6 was concocted to simultaneously reproduce the counting rate measurements of DEMETER and produce an estimate of the induced precipitation at a specific energy and location. This exercise was nominally successful, but the results cannot be used as a check against the magnitude of the precipitation flux predicted by the model of this section. The reason is that even if a PAD is constricted to reproduce the DEMETER measurements, the shape and absolute level of its near loss cone distribution can still be manipulated to give a wide range of precipitation fluxes. This behavior is greatly accentuated by a low RMS pitch angle change like our 0.001°. For example, two feasible near loss cone edges for the shifted PAD are $10^{-4}\sin^{0.2}(\gamma_1)$ and $10^{-3}\sin(\gamma_1)$. While both of these reproduce the background CR typically measured by DEMETER, the former produces ~600 times the precipitation flux for our RMS pitch angle change. The shifted PAD used in section 4 produced a precipitation flux of $\sim 10^{-4}$ cm^{-2} s^{-1} keV^{-1}, which is in approximate agreement with the model of this section for the same $L = 2.0$, $E = 130$ keV, but this agreement is mostly coincidental.

[31] Even though the limitations of the experiment prevent us from determining the actual magnitude of the precipitation flux, DEMETER observations can still provide inputs on its key determining factors, which are the RMS pitch angle change and the near loss cone pitch angle distribution. The RMS pitch angle change calculated using the formulations of *Inan et al.* [1978] and used by the model of this section reproduce the DEMETER measurements. While this agreement is still closely tied to the use of a configurable PAD, this result is nevertheless encouraging. The other key factor, the near loss cone distribution, can be restricted in scale and shape to those combinations which can produce the range of counting rates measured by DEMETER. As discussed in section 4, the typical IDP counting rates presented in Figure 7 suggest that a square PAD should be scaled by $\sim 10^{-4}$ relative to AE8, and that a sine PAD should be scaled by $\sim 10^{-3}$. This result can be directly compared to the model predictions presented by *Inan et al.* [2007b], which used a square PAD with scaling based on the work of *Bell et al.* [2002]. For $L = 2$ and energies near 100 keV, the scaling by *Bell et al.* [2002] is about 100 times less than that of AE8. Therefore the square PAD by *Inan et al.* [2007b] is effectively a steep, scaled down near loss cone distribution much like the tale of the shifted PAD of Figure 6d. Since it is only the edge of the loss cone that matters for the purposes of absolute value of

precipitation when the RMS pitch angle change is low, this choice is reasonable. However, a square PAD should be scaled by $\sim 10^{-4}$ relative to AE8, not just 10^{-2}, to represent a typical near loss cone edge. This scaling means that the results of *Inan et al.* [2007b] are more applicable to the $\sim$3% of the days for which near loss cone flux is markedly higher and a 10^{-2} scaling with respect to AE8 would agree with DEMETER measurements of background flux densities in the NPM precipitation region. Since the modeling presented by *Inan et al.* [2007b] showed agreement with the few strongest cases of subionospheric detection of transmitter-induced precipitation, it is encouraging that the scaling of its near loss cone population matches what we see here to be the few cases most conducive to strong precipitation events.

[32] While the above analysis of the magnitude of the precipitation flux is very convoluted and limited, the energy spectrum of the precipitation bursts detected by DEMETER can be compared more directly to the model. The energy spectra of 29 December 2005 were presented in Figure 5 for periods near L = 1.97. Figure 5b shows an NPM-induced increase of 0.12 $cm^{-2}s^{-1}keV^{-1}$ near 130 keV. The flux bursts detected by DEMETER are at energies higher than the model predicts. This result may suggest higher numbers of more energetic electrons in the trapped electron energy spectra, or that the cold plasma density is lower than modeled leading to an increase in resonant energy. For example, if the cold plasma density is simply scaled by 2/3, then the energy of peak precipitation for L = 1.9 changes from 98 keV to 136 keV. These scenarios could explain the detection of a 130 keV precipitation peak near L = 1.97 as seen on 29 December 2005, and the detection of a 220 keV precipitation peak near L = 2.0 as seen on 3 September 2007. The 3 September 2007 case, however, should not be compared directly to the model results because it is a case of detection in the conjugate region while the model results are specific to the northern precipitation region. While the precise energies appear to be high in these cases, it should be noted that detection at lower energies is largely prevented by the presence of high background flux. Additionally, it is encouraging that the energies of the energetic electron bursts decrease with increasing L for the cases of 29 December 2005 and 20 February 2008. The model predicts a similar rate of decrease in energy. The electron bursts detected on 3 September 2007, which did not change in energy by a discernible amount, did not follow this trend. However, considering the 8.9 keV energy resolution of the electron flux measurements and the expected change of $\sim$10–20 keV over the $\sim$0.04 change in L, the lack of discernible change in energy is within the error of this comparison.

[33] The model predicts that the onset delay of precipitation following the commencement of an NPM ON transmission should be less than a quarter of a second for the northern hemisphere, and another quarter of a second for the conjugate. These delays closely reflect the approximate quarter second bounce period of a 100 keV electron at L = 2.0, and the group traveltime of the NPM signal to the geomagnetic equatorial region where most of the pitch angle scattering occurs. The one second time resolution of the IDP prevents a precise measurement of this delay, but most bursts tend to appear with a 1–3 sec delay. The lengthy delay may be the result of pitch angle scattering requiring multiple interactions to fill the IDP viewing window to the point that detection can occur. Since the IDP views trapped particles, as particles at higher pitch angles outside the IDP viewing window undergo multiple bounces and are scattered multiple times, the IDP viewing window may be gradually filled until detection finally occurs at a delayed time. This is one possible explanation for the increase in onset delay, but by itself it is still insufficient because the bursts in energetic particle flux that DEMETER detects do not appear gradually, but rather are delayed and then appear abruptly. This observed behavior would suggest a PAD which is shifted slightly further from the IDP viewing window than the simulated PAD in Figure 6d. For such a PAD, multiple resonant interactions would be required before the pitch angle scattered electrons appear in the IDP viewing window. Another explanation (one that could explain both the high energy and the lengthy onset delay) is that the detected flux bursts are the result of pitch angle scatter by the wave that has already reflected off the conjugate ionosphere and is propagating back along the magnetic field line. This reflected wave would have a smaller component of its wave vector parallel to the magnetic field line, leading to a higher resonance energy, and would also interact with particles at a later time than would the initial wave. In agreement with this possibility is the fact that Doppler shifted NPM pulses were observed on both the 29 December 2005 and 3 September 2007 cases when significant onset delay occurred, but a Doppler shifted NPM pulse was not observed on 20 February 2008 when the onset delay was much shorter.

[34] Despite the minor disagreements with the best-case experimental results, the model is still in agreement with the general result that NPM-induced precipitation should rarely be detected onboard DEMETER. The minimum energy particle detectable by DEMETER is 72.9 keV, and the background flux detected in the 72.9–100 keV energy range is consistently very high, effectively preventing the analysis of small perturbations of precipitation bursts below 100 keV. Additionally, for a precipitation event to be detected by DEMETER in the 100–200 keV range near L = 2.0, an increase in energetic electron flux on the order of 1 $cm^{-2}s^{-1}str^{-1}keV^{-1}$ or greater is required. Such an increase requires either very specific PADs or transmitter-induced precipitation of quantities much higher than those predicted by simulation, and thus should only occur on rare occasions. Given that even a single burst of such precipitation events is observed on less than 15% of the passes, it is likely that the majority of the scattering events induced by NPM are simply below the level of detection for the IDP instrument, due largely to its orientation.

6. Discussion and Future Work

[35] The detection of consecutive bursts of near loss cone energetic electron flux which correlate with NPM transmissions suggest that NPM induced significant precipitation at those times and that DEMETER successfully detected the signatures of those events. Counting only two-burst events, detection occurred on only 2.6% of the DEMETER passes. If both one-burst and two-burst events are counted, the detection rate is still only 13.9%. Despite the low rate of

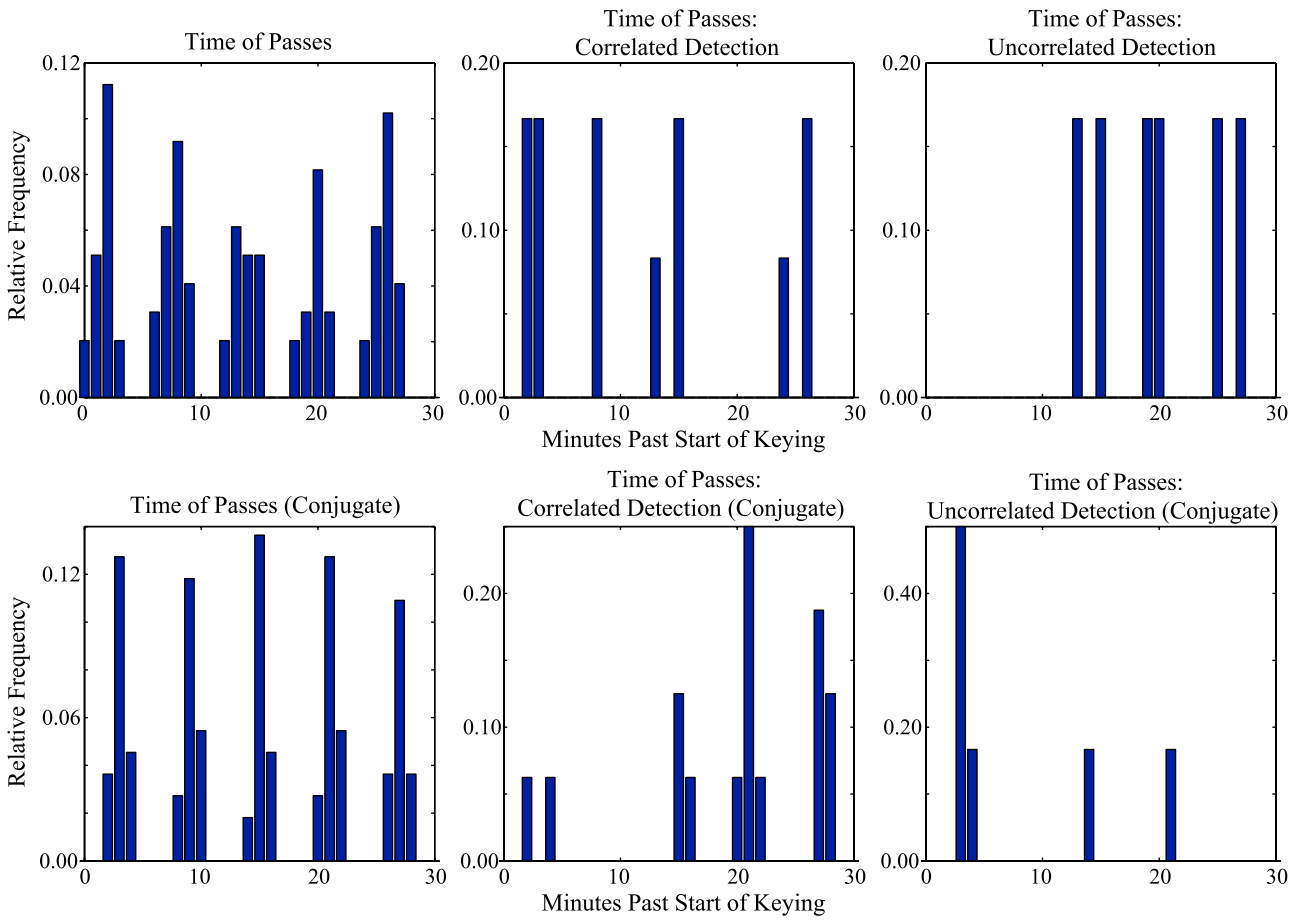

Figure 9. Distribution of times of DEMETER passes through the precipitation region and its conjugate with respect to the start of each NPM keying session.

detection, the results are in general agreement with model predictions. Based on the low detection rate, it is possible that NPM did not effectively precipitate particles on a regular basis. Even if NPM routinely induced precipitation, however, DEMETER would only detect the event in the cases of a particular initial PAD, and if the energies and levels of the pitch angle scattering were at slightly greater values than those predicted by the models of *Kulkarni et al.* [2008] and *Bortnik et al.* [2006].

[36] It was concluded by *Inan et al.* [2007b] that NPM frequently induced precipitation during the course of experimentation. This conclusion was drawn following the repeated keying of the NPM transmitter in an ON-OFF format and the observation of the same periodicity in the amplitude and phase of the subionospherically propagating signals of the 24.8 kHz NLK (Jim Creek, Washington) and 25.2 kHz NLM (LaMoure, North Dakota) transmitters at Midway Island. It was argued that this technique provides an indirect detection of precipitation that the precipitation induces secondary ionization in the ionosphere which perturbs the propagation of subionospheric VLF signals. A satellite with an energetic particle detector passing through the precipitation region should provide a more direct measurement of induced precipitation, but the DEMETER satellite rarely detected NPM induced precipitation over the course of many of the same NPM transmission periods. It has been shown, however, that even cases of significant precipitation may not be detectable by DEMETER with its configuration of detector orientation. Therefore the lack of consistent detection of NPM induced precipitation with DEMETER fails to either support or refute the claim that NPM routinely induces precipitation.

[37] The reason for the low detection rate of NPM-induced precipitation has been explained by the low levels and energies to be expected for NPM-induced precipitation as discussed in section 5, in conjunction with the confounding factor of the IDP viewing window as discussed in section 4. An additional factor is the large differential between the bounce and drift loss cones at the longitude of NPM. This differential means that few particles may reside near the loss cone and significant cumulative scattering may be required in order to induce detectable flux increases. Instances of geomagnetic activity could populate this region of the pitch angle distribution, but no significant correlation was found between geomagnetic activity and instances of precipitation. (It should be noted, however, that very little significant geomagnetic activity occurred during the course of the experiment, and that the Kp and Dst indices used for comparison may not be localized enough for the required analysis.)

[38] It is unclear what facilitated detection in the few cases that it did occur. Increased coupling of VLF wave power into the magnetosphere could increase pitch angle scattering, but the power of the NPM signal as detected

onboard DEMETER was no higher than usual for the cases of detection. Geomagnetic activity or lightning west of NPM could prime the PAD for detection, but, based on the Kp and Dst indices and samples of lightning activity from LIS (Lightning Imaging Sensor) data [*Christian et al.*, 1999; *Boccippio et al.*, 2002; *Christian et al.*, 2003], there was nothing unique about the times when detection did occur. The detection of a Doppler shifted NPM pulse in the northern region would suggest that the wave has reflected off the conjugate ionosphere and traversed the magnetosphere with increased wave normal angle. As was suggested in section 5, this reflected wave may induce the cases of pitch angle scattering which are detected by DEMETER with a lengthy onset delay. However, such Doppler shifted pulses are detected on nearly every pass, so this is not a characteristic that can be unique to the cases of detection. Since the shape of the PAD near the IDP viewing window is so critical to detection, it is suspected that the cases of detection benefited from a favorable PAD, but it is unclear what would have established those conditions.

[39] The one-shot detection case of 20 February 2008, where NPM turned ON after a full minute of being OFF and a significant increase in energetic particle flux immediately followed, may illustrate the behavior near the loss cone in the PAD. Even when NPM is not transmitting a specific ON-OFF format for these experiments, the transmitter is typically ON transmitting modulated signals for its regular message traffic so that the near loss cone region may always be populated by the resultant scattering. The minute of off time on this day may have allowed this region to empty so that a significant increase was witnessed when NPM was turned back ON. On the other hand, the NPM signal typically transmits in an MSK (Minimum Shift Keying) format when it is not being keyed for these experiments, and even though NPM is ON prior to the initiation of a keying session, its signal may be less effective at pitch angle scattering. The scattering efficiency of the MSK modulated signal is not known, but this consideration lends itself to future analysis of the temporal development of the PAD throughout the keying session. Figure 9 presents the times of the DEMETER passes through the precipitation region and its conjugate with respect to the start of each keying session, along with the times for passes which showed correlated and uncorrelated detection. The times of the passes are clumped due to the nature of DEMETER orbits, but they are still well spread throughout the 30-min window. The results evade a simple interpretation, but they are further suggestive that an analysis of the temporal development of the PAD could produce additional insight. Future work on this NPM region data set is likely to include the analysis of the subionospheric detection data using new techniques to further examine the temporal development of the PAD.

[40] Experiments with the NPM transmitter constitute the first in a series of transmitter-induced precipitation experiments. Similar experiments began in the Summer of 2008 with the 24 kHz NAA transmitter (44.7°N, 67.3°W, $L = 2.8$) located in Cutler, ME. Experiments are also planned with the 19.8 kHz NWC transmitter (21.8°S, 114.2°E, $L = 1.4$) of North West Cape, Australia. Both subionospheric and satellite-based detection methods are arranged for these experiments. These experiments, with their wide range of transmitter L shells and bounce-drift-loss cone differentials, would significantly add to the global picture of transmitter-induced precipitation and provide opportunities to attempt more of the special transmission formats which showed promise with NPM.

[41] **Acknowledgments.** The Stanford portion of this work was supported by a William R. and Sara Hart Kimball Stanford Graduate Fellowship and by the Defense Advanced Research Projects Agency (DARPA) and the High Frequency Active Auroral Research Projects Agency (HAARP) under ONR grants N00014-06-1-1036 and N00014-05-1-0854-NCX to Stanford University. Special thanks to the NPM operators and U.S. Fish and Wildlife Service on Midway Island for the transmissions and data collection.

[42] Zuyin Pu thanks the reviewers for their assistance in evaluating this paper.

References

Abel, B., and R. M. Thorne (1998), Electron scattering loss in Earth's inner magnetosphere: 1. Dominant physical processes, *J. Geophys. Res.*, *103*(A3), 2385–2396.

Anderson, R. R. (1976), Wave particle interactions in the evening magnetosphere during geomagnetically disturbed periods, Ph.D. thesis, The Univ. of Iowa, Iowa City, Iowa.

Bell, T. F., U. S. Inan, J. Bortnik, and J. D. Scudder (2002), The Landau damping of magnetospherically reflected whistlers within the plasmasphere, *Geophys. Res. Lett.*, *29*(15), 1733, doi:10.1029/2002GL014752.

Boccippio, D. J., W. J. Koshak, and R. J. Blakeslee (2002), Performance assessment of the optical transient detector and lightning imaging sensor. Part I: Predicted diurnal variability, *J. Atmos. Ocean. Technol.*, *19*, 1318–1332.

Bortnik, J., U. S. Inan, and T. F. Bell (2006), Temporal signatures of radiation belt electron precipitation induced by lightning-generated MR whistler waves: 1. Methodology, *J. Geophys. Res.*, *111*, A02204, doi:10.1029/2005JA011182.

Brinca, A. (1972), On the stability of obliquely propagating whistlers, *J. Geophys. Res.*, *77*, 3495–3507.

Carpenter, D. L., and R. R. Anderson (1992), An ISEE/whistler model of equatorial electron density in the magnetosphere, *J. Geophys. Res.*, *97*(A2), 1097–1108.

Christian, H. J., et al. (1999), The Lightning Imaging Sensor, in *Proceedings of the 11th International Conference on Atmospheric Electricity*, pp. 746–749.

Christian, H. J., et al. (2003), Global frequency and distribution of lightning as observed from space by the optical transient detector, *J. Geophys. Res.*, *108*(D1), 4005, doi:10.1029/2002JD002347.

Friedel, R. H. W., G. D. Reeves, and T. Obara (2002), Relativistic electron dynamics in the inner magnetosphere — a review, *J. Atmos. Sol.-Terr. Phys.*, *64*, 265–282.

Imhof, W. L., et al. (1983), Direct observation of radiation belt electrons precipitated by controlled injection of VLF signals from a ground-based transmitter, *Geophys. Res. Lett.*, *10*(4), 361–364.

Imhof, W. L., R. R. Anderson, J. B. Reagan, and E. E. Gaines (1981), The significance of VLF transmitters in the precipitation of inner belt electrons, *J. Geophys. Res.*, *86*(A13), 11,225–11,234.

Inan, U. S. (1977), Non-linear gyroresonant interactions of energetic particles and coherent VLF waves in the magnetosphere, Ph.D. thesis, Stanford Univ., Stanford, Calif.

Inan, U. S. (1987), Gyroresonant pitch angle scattering by coherent and incoherent whistler mode waves in the magnetosphere, *J. Geophys. Res.*, *92*(A1), 127–142.

Inan, U. S., and T. F. Bell (1977), The plasmapause as a VLF wave guide, *J. Geophys. Res.*, *83*(19), 2819–2827.

Inan, U. S., D. Piddyachiy, W. B. Peter, J. A. Sauvaud, and M. Parrot (2007a), DEMETER satellite observations of lightning-induced electron precipitation, *Geophys. Res. Lett.*, *34*, L07103, doi:10.1029/2006GL029238.

Inan, U. S., et al. (2007b), Subionospheric VLF observations of transmitter-induced precipitation of inner radiation belt electrons, *Geophys. Res. Lett.*, *34*, L02106, doi:10.1029/2006GL028494.

Inan, U. S., T. F. Bell, and R. A. Helliwell (1978), Nonlinear pitch angle scattering of energetic electrons by coherent VLF waves in the magnetosphere, *J. Geophys. Res.*, *83*(A7), 3235–3253.

Inan, U. S., H. C. Chang, R. A. Helliwell, W. L. Imhof, J. B. Reagan, and M. Walt (1985), Precipitation of radiation belt electrons by man-made waves: A comparison between theory and measurement, *J. Geophys. Res.*, *90*(A1), 359–369.

Koons, H. C., B. C. Edgar, and A. L. Vampola (1981), Precipitation of inner zone electrons by whistler mode waves from the VLF transmitters UMS and NWC, *J. Geophys. Res.*, *86*(A2), 640–648.

Kulkarni, P., U. S. Inan, T. F. Bell, and J. Bortnik (2008), Precipitation signatures of ground-based VLF transmitters, *J. Geophys. Res.*, *113*, A07214, doi:10.1029/2007JA012569.

Lauben, D. S., U. S. Inan, and T. F. Bell (2001), Precipitation of radiation belt electrons induced by obliquely propagating lightning-generated whistlers, *J. Geophys. Res.*, *106*(A12), 29,745–29,770.

Lehtinen, N. G., and U. S. Inan (2008), Radiation of ELF/VLF waves by harmonically varying currents into a stratified ionosphere with application to radiation by a modulated electrojet, *J. Geophys. Res.*, *113*, A06301, doi:10.1029/2007JA012911.

Lyons, L. R., and D. J. Williams (1975), The quiet time structure of energetic (35-560 keV) radiation belt electrons, *J. Geophys. Res.*, *80*(7), 943–950.

Parrot, M. (2006), Special Issue: First results of the DEMETER microsatellite, *Planet. Space Sci.*, *54*(5), 411–558.

Ristic-Djurović, J. L., T. F. Bell, and U. S. Inan (1998), Precipitation of radiation belt electrons by magnetospherically reflected whistlers, *J. Geophys. Res.*, *103*(A5), 9249–9260.

Sauvaud, J. A., et al. (2006), High energy electron detection onboard DEMETER: The IDP spectrometer, description and first results on the inner belt, *Planet. Space Sci.*, *54*(5), 502–511, doi:10.1016/j.pss.2005.10.019.

Sauvaud, J. A., R. Maggiolo, C. Jacquey, M. Parrot, J. J. Berthelier, R. J. Gamble, and C. J. Rodger (2008), Radiation belt electron precipitation due to VLF transmitters: Satellite observations, *Geophys. Res. Lett.*, *35*, L09101, doi:10.1029/2008GL033194.

Shprits, Y. Y., S. R. Elkington, N. P. Meredith, and D. A. Subbotin (2008a), Review of modeling of losses and sources of relativistic electrons in the outer radiation belt: I. Radial transport, *J. Atmos. Sol.-Terr. Phys.*, *70*, 1679–1693.

Shprits, Y. Y., D. A. Subbotin, N. P. Meredith, and S. R. Elkington (2008b), Review of modeling of losses and sources of relativistic electrons in the outer radiation belt: II. Local acceleration and loss, *J. Atmos. Sol.-Terr. Phys.*, *70*, 1694–1713.

Starks, M. J., T. F. Bell, R. A. Quinn, U. S. Inan, D. Piddyachiy, and M. Parrot (2009), Modeling of Doppler-shifted terrestrial VLF transmitter signals observed by DEMETER, *Geophys. Res. Lett.*, doi:10.1029/2009GL038511, in press.

Vampola, A. L. (1977), VLF transmission induced slot electron precipitation, *Geophys. Res. Lett.*, *4*(12), 569–572.

Walt, M. (1994), *Introduction to Geomagnetically Trapped Radiation*, Cambridge Univ. Press, New York.

K. L. Graf, U. S. Inan, P. Kulkarni, and D. Piddyachiy, Space, Telecommunications and Radioscience Laboratory, Stanford University, 350 Serra Mall, Room 351, Stanford, CA 94305, USA. (graf@stanford.edu)

M. Parrot, Laboratoire de Physique et Chimie de l'Environnement, Centre National de la Recherche Scientifique, 3A Avenue de la Recherche, 45071 Orléans, cedex 2 France.

J. A. Sauvaud, Centre d'Etude Spatiale des Rayonnements, Centre National de la Recherche Scientifique, 9 avenue du Colonel Roche, 31028 Toulouse, cedex 4 France.